Measurements of morphology and refractive indexes on human downy hairs using three-dimensional quantitative phase imaging

SangYun Lee
Kyoohyun Kim
Yuhyun Lee
Sungjin Park
Heejae Shin
Jongwon Yang
Kwanhong Ko
HyunJoo Park
YongKeun Park

Measurements of morphology and refractive indexes on human downy hairs using three-dimensional quantitative phase imaging

SangYun Lee,[a] Kyoohyun Kim,[a] Yuhyun Lee,[b] Sungjin Park,[b] Heejae Shin,[b] Jongwon Yang,[b] Kwanhong Ko,[b] HyunJoo Park,[a] and YongKeun Park[a,*]
[a]Korea Advanced Institute of Science and Technology, Department of Physics, 291 Daehak-Ro Yusung-Gu, Daejeon 305-701, Republic of Korea
[b]Daejeon Dongsin Science High School, 423 Okcheon-Ro Dong-Gu, Daejeon 300-310, Republic of Korea

Abstract. We present optical measurements of morphology and refractive indexes (RIs) of human downy arm hairs using three-dimensional (3-D) quantitative phase imaging techniques. 3-D RI tomograms and high-resolution two-dimensional synthetic aperture images of individual downy arm hairs were measured using a Mach–Zehnder laser interferometric microscopy equipped with a two-axis galvanometer mirror. From the measured quantitative images, the RIs and morphological parameters of downy hairs were noninvasively quantified including the mean RI, volume, cylinder, and effective radius of individual hairs. In addition, the effects of hydrogen peroxide on individual downy hairs were investigated. © *2015 Society of Photo-Optical Instrumentation Engineers (SPIE)* [DOI: 10.1117/1.JBO.20.11.111207]

1 Introduction

Human body hairs exhibit distinct morphologies at their relative sites in the body, from soft downy hairs on the arms to long stiff hairs on the head. The characteristics of different hairs have been regarded as one of the evolutionary consequences incurred by human bipedalism.[1,2] While human body hairs have lost their thermoregulatory roles in maintaining warmth through an evolutionary process, the decorative aspects of hair have gained attention and led many researchers to investigate the microstructures of hairs using diverse microscopic techniques, including atomic force microscopy,[3–5] scanning electron microscopy,[6–8] transmission electron microscopy,[9,10] confocal microscopy,[11,12] infrared spectroscopy,[13–15] optical reflectometry,[16] and ellipsometry[17] under various experimental conditions. Using an inverse Monte-Carlo method, the melanin contents of human hairs have been quantitatively estimated from digital images.[18] Chemical analyses of hairs for drug detection (e.g., alcohol and cocaine) also have been extensively carried out, particularly in the fields of forensic science.[19–23] However, previous approaches have difficulties in providing simultaneous measurements of three-dimensional (3-D) morphologies and the refractive index (RI) of hairs quantitatively and noninvasively. Furthermore, most previous studies have used expensive instrumentation, which prevents these imaging techniques from being utilized in general laboratories in which body hairs are studied.

Here, we present quantitative phase imaging (QPI) as an effective imaging tool to study the morphological and optical properties of downy hairs in a noninvasive and quantitative manner. QPI techniques provide quantitative measurements of optical phase delay introduced by intrinsic RI distributions of transparent cells using interferometry.[24,25] QPI techniques have been applied previously for biological studies of cells and tissues including blood cells,[26–33] cell growth monitoring,[34] neurons,[35] and optical imaging of tissue slices.[36] The feasibility of noninvasive and quantitative imaging of QPI was demonstrated with individual downy hairs using the QPI techniques. The high-resolution two-dimensional (2-D) holographic synthetic aperture images and 3-D RI distribution maps of individual hairs were measured, from which the morphological and biochemical properties were retrieved, including the mean RI, volume, cylinder, and effective radius of individual hairs. Furthermore, we investigated the effects of hydrogen peroxide (H_2O_2), which is one of the widely-used hair bleaching agents, on individual downy hairs using the present method.

2 Materials and Methods

2.1 Sample Preparations

A total of 13 human downy hairs were collected from one arm of a healthy donor (Asian male) [Fig. 1(a1)]. Each hair was gently posed on the top of a coverslip (24×50 mm², C024501, Matsunami, LTD, Japan) with oil immersion ($n = 1.518$), which decreases the RI contrast between the hairs and the medium. The sample was then covered with another coverslip [Fig. 1(a2)]. To study the effects of hydrogen peroxide on the hair structures, four hair samples were treated with 3% H_2O_2 solution (Sigma–Aldrich, St. Louis, Missouri) for 24 h. The shape of the edges of the hairs cells were imaged before and after the H_2O_2 treatments.

---

*Address all correspondence to: YongKeun Park, E-mail: yk.park@kaist.ac.kr

2.2 Optical Setup for Quantitative Phase Imaging

For quantitative measurements of human downy hairs, we employed a Mach–Zehnder interferometric microscope equipped with a two-axis galvanometer mirror.[37–39] The schematic of the setup is shown in Fig. 1(b). A diode-pumped solid state laser ($\lambda = 532$ nm, 50 mW, Cobolt Co., Solna, Sweden) is used as a coherent light source. A beam splitter (BS, BS016, Thorlabs) divides a laser beam into two arms: a reference beam and a sample beam. The sample beam passes through a downy hair loaded on the sample stage of an inverted microscope. A two-axis galvanometer mirror (GM, GVS012/M, Thorlabs) varies the angle of the illumination beam impinging onto the hair sample, from which 2-D optical field images of the sample are obtained with various illumination angles. For the reconstruction of off-axis interference patterns, the reference and the sample beams are recombined with a tilted angle by another beam splitter, and the resultant interferograms of the samples are recorded by a high-speed CMOS camera (Neo sCMOS, Andor Inc., Northern Ireland, UK).

An objective lens [UPLFLN, 60×, numerical aperture (NA) = 0.9, Olympus Inc., San Diego, California] was used as a condenser lens with the tube lens of a focal length of 200 mm. For the imaging purpose, a high-NA objective lens (PLAPON, 60×, oil immersion, NA = 1.42, Olympus Inc., San Diego, California) was used with an additional telescopic 4-f system, and the total magnification of the imaging system is 250×. The camera has 1776×1760 pixels with a pixel size of 6.5 μm. The full field of view at the sample plane was 46.18×45.76 μm^2, considering the total magnification of 250×. Each hair sample was illuminated with plane waves at 300 different incidence angles, which were systematically controlled by the two-axis GM at a frame rate of 100 Hz.

2.3 Image Reconstruction Procedures

Complex optical fields of the sample were retrieved from the interferogram recorded by the QPI technique, via a retrieval algorithm based on Fourier transform.[40,41] The phase and amplitude maps of a representative hair are shown in Figs. 1(c1) and 1(c2).

From a set of retrieved phase images [Fig. 1(c1)] with various illumination angles, the 2-D high-resolution synthetic aperture phase image [Fig. 1(c3)] was constructed with a synthetic aperture imaging algorithm.[42,43] By numerically extending the aperture size, the synthetic aperture algorithm fully used the high-spatial frequency information of a sample which cannot be accessed with just a single laser illumination angle. The numerical extension of an aperture was conducted in the 2-D Fourier space, and the resultant 2-D synthetic aperture phase image [Fig. 1(c3)] exhibited a higher-spatial resolution and signal-to-noise ratio (SNR), compared to the phase image from a single hair interferogram [Fig. 1(c1)].[44,45]

In principle, the resolution of an imaging system is determined by the NAs of an objective lens. In general, for 2-D QPI with a single illumination, the maximum accessible spatial frequency $|k_{max}|$ is determined as $2\pi NA_{imag}/\lambda$, where NA_{imag} represents the NA of the imaging system. In synthetic aperture imaging, the maximum spatial frequency can be further extended by combining multiple phase images obtained with various incident angles; the maximum spatial frequency is extended to $2\pi(NA_{imag} + NA_{illum})/\lambda$, where NA_{illum} is the NA of the condenser lens. The SNR of the synthetic aperture phase image is also more significantly enhanced than that of a single phase image, mainly due to speckle noise reduction.

A differential interference contrast (DIC) image can also be numerically reconstructed from the synthetic aperture phase
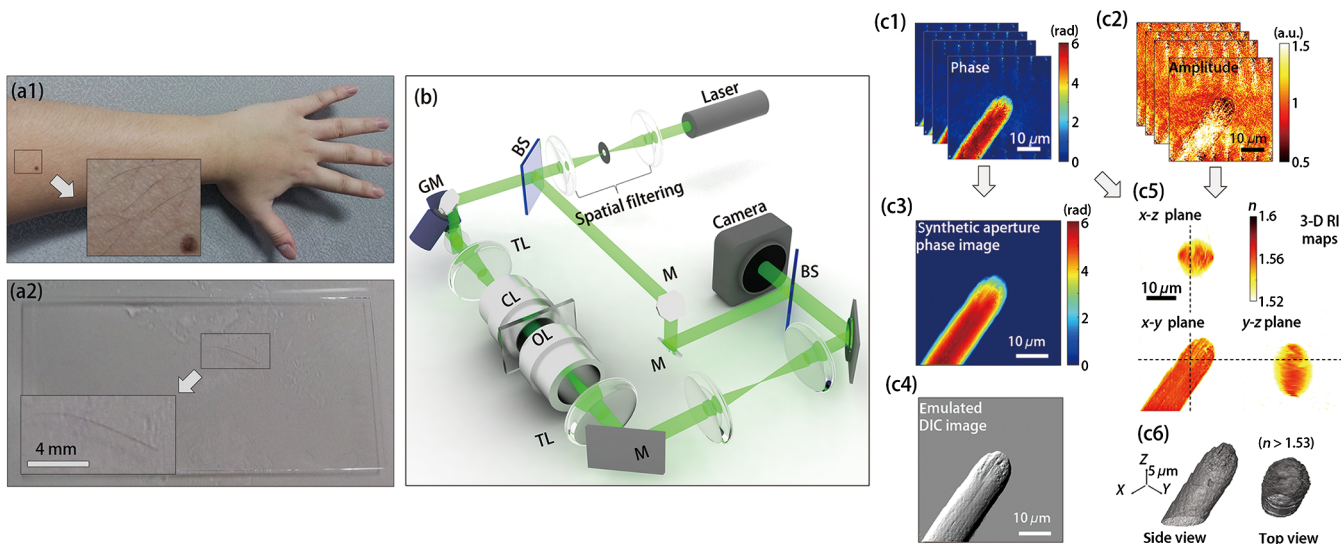

Fig. 1 (a) Human downy hair preparation. (a1) Left arm of a healthy donor from which downy hairs were collected. (a2) A downy hair with immersion oil loaded between two coverslips. (b) Mach–Zehnder interferometric microscopy equipped with a two-axis galvanometer mirror. BS, beam splitter; GM, galvanometer mirror; CL, condenser lens; OL, objective lens, M, mirror. (c) Holographic image reconstruction process. A set of retrieved (c1) phase and (c2) amplitude maps of complex optical fields. (c3) Synthetic aperture phase image. (c4) Emulated differential interference contrast (DIC) image. (c5) Reconstructed three-dimensional refractive index (3-D RI) distributions of a hair sample. (c6) 3-D RI isosurface of a hair tomogram.

image [Fig. 1(c4)]. This emulated DIC image is readily obtained from a synthetic aperture phase image by numerically interfering an original phase image and a slightly translated synthetic aperture phase image with an additional phase shift.[46] Because the optical imaging contrast in DIC images is a result of the phase gradient, the imaging contrast is enhanced for objects with high RI changes or gradients, such as subcellular organelles in unstained biological cells or defects in nonbiological samples.

To reconstruct the 3-D RI distribution of a hair sample from a set of retrieved complex optical fields, we used the optical diffraction tomography (ODT) algorithm.[39,47–49] Compared to the projection algorithm,[50,51] the ODT algorithm considers light diffraction at samples, and thus, provides high-resolution tomographic reconstruction with better image qualities, especially for large samples with high RI contrast.[48]

2.4 Statistical Analysis

P-values are calculated by two-tailed paired *t*-test comparing quantitative parameters of human arm hairs. All the numbers following the $\pm$ sign in the text are standard deviations (SD).

3 Result and Discussion

3.1 High-Resolution Two-Dimensional Phase Images and Three-Dimensional Refractive Index Maps of Human Downy Hairs

In order to measure the morphologies of individual downy hairs, we measured and took 3-D RI maps and 2-D synthetic aperture phase images of human downy hairs collected from arms, using the Mach–Zehnder laser interferometry equipped with a

two-axis galvanometer mirror (see Sec. 2). Figure 2 shows the measured images of representative human downy hairs. Measured hair samples were categorized into two groups based on their morphologies; hairs in the soft type exhibit smooth surfaces and internal RI distributions [Figs. 2(a1)–2(a3)], and hairs in the rough type present complex internal structural defects and spiky surfaces [Figs. 2(b1)–2(b3)].

High-resolution 2-D synthetic aperture phase images [Figs. 2(a1) and 2(b1), top], corresponding emulated DIC images [Figs. 2(a1) and 2(b1), bottom] and three cross-sectional slices of the reconstructed 3-D RI tomograms [Figs. 2(a2) and 2(b2)] of the representative downy hairs showed significant morphological differences (see Sec. 2). The renderings of 3-D RI isosurfaces ($n > 1.545$) of the hair samples are also shown in Figs. 2(a3) and 2(b3).

In total, 13 human downy hairs were measured; six hair cells were categorized as the soft type, and seven hair cells were in the rough type. The representative holographic images of the soft type hair [Figs. 2(a1)–2(a3)] had soft and continuously connected cell boundaries without any apparent structural defects. The relatively homogenous RI distribution of the soft type hair [Fig. 2(a2)] reflects the homogeneity of its internal structures. Figures 2(b1)–2(b3) show quantitative phase images of the representative rough type downy hair.

Significantly low speckle noise level in the backgrounds of the DIC image indicates that the observed fine structures in the hair sample are from real structural defects. The characteristic fine structures, indicated with the colored arrows in Fig. 2(b1), are also shown in the reconstructed 3-D RI tomogram [Fig. 2(b2)]. Particularly, the structural defect [the black arrow in Fig. 2(b1)] can be clearly seen in the *z*-*y* sectional RI slice. Finally, the RI isosurface of the rough type hair [Fig. 2(b3)] shows more
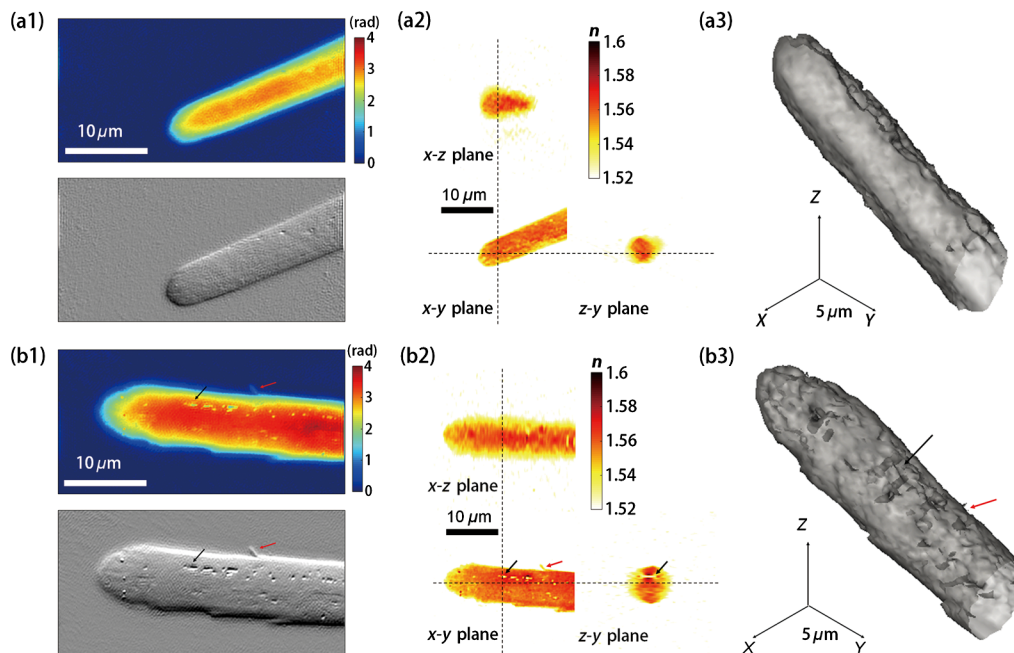

Fig. 2 (a) and (b) Quantitative phase images of representative human downy hairs for soft and rough type: (a1) and (b1) the two-dimensional synthetic aperture phase image (top) and the corresponding emulated DIC image (bottom) of the representative hair samples. (a2) and (b2) The cross-sectional slices of the reconstructed 3-D RI tomogram in *x*-*y*, *z*-*y*, and *x*-*z* plane. (a3) and (b3) Perspective view of the representative 3-D hair RI isosurface. RI threshold set as a value of 1.545. Each colored arrow in the figures represents the same fine structures of the measured downy hair.

complicated surface structures when compared to the RI isosurface of the soft type hair [Fig. 2(a3)].

3.2 Retrieval of Quantitative Downy Hair Parameters

To demonstrate the quantitative imaging capability of the present method for the study of downy hairs, we retrieved the RIs and morphological parameters from measured 3-D RI maps of individual hairs. The retrieved parameters included mean RI values, the volumes for 20-μm length hairs [Fig. 3(a)], cylindrical radii of the hairs as a function of length [Fig. 3(b)], and the effective radii of hair edges [Fig 3(c)].

To obtain the mean RI value of a hair, we averaged the RI values over the sample area in the focal plane [i.e., the x-y plane in Figs. 2(a2) and 2(b2)]. Volumes of the 20-μm length hairs were calculated by integrating voxels higher than the RI threshold ($n = 1.53$). The mean values of the retrieved mean RI at 532 nm and volume for the 20-μm length hairs were 1.557 ± 0.007 (mean $\pm$ SD) and 692 ± 173 femtoliter (fL), respectively, which are in good agreement with a previous RI measurement.[52]

The cylindrical radii of hairs as a function of hair lengths are retrieved assuming a cylindrical symmetry [inset in Fig. 3(b)]. Then the cylinder radius represents the hair thickness as a function of hair length. The graph in Fig. 3(b) depicts the measured cylindrical radii for 13 downy hairs along their hair axis. The red line denotes the mean cylinder radii, and the shaded region corresponds to SD. The mean cylindrical radii seem to saturate beyond a length of 5 μm.

The roundness of the hair tips can be effectively described by measuring the effective radii of the tips [Fig. 3(c)]. In order to retrieve the effective radius of a hair R, the following relation was used: $R = (r^2 + h^2)/2h$, where r is the radius of a circular slice orthogonal to the hair axis, h is the distance between the circular slice and the hair tip. For the case of a perfect sphere, any circular slice of the sphere with a different h gives the same R. This is not the case for hairs, and the height h should be determined appropriately in order to have a sphere with an effective radius R_{eff} describing the roundness of the hair edge. We determined h from the plane on the hair axis where the cylindrical radius equals 85% of the saturated cylindrical radius. Results are shown in Fig. 3(c). The mean effective radius of the measured hairs was 3.00 ± 0.37 μm.

To address the relationship between the effective radii R_{eff} and the saturated cylindrical radii of the hairs r_{sat}, the correlation of these two parameters were investigated [Fig. 3(d)]. The correlation clearly shows a linear relationship; they are well described by a linear regression model $R_{\text{eff}} = 0.79\ r_{\text{sat}} + 0.26$ μm with $R^2 = 0.96$. This linear relation of these radii implies that each human arm hair shares a morphological similarity with each other. In addition, a coefficient of proportionality less than one means that hair edges are sharper than ideal hemispheres, in accordance with the measured 3-D RI tomograms.

3.3 Effects of Hydrogen Peroxide on Individual Human Downy Hairs

To further show the capability of QPI, we performed experiments to study the effects of hydrogen peroxide on individual
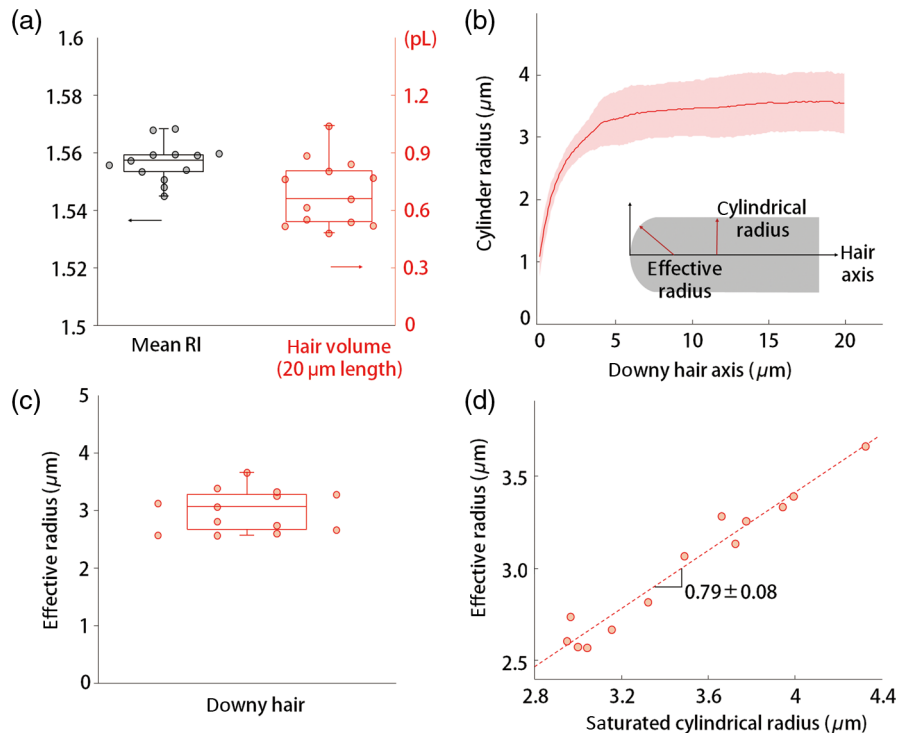

Fig. 3 RIs and morphological parameters of human downy hairs. (a) Retrieved mean RIs and volumes of 20-μm length hairs. (b) Cylindrical radii of hairs as a function of length. The shaded area represents standard deviations. Inset: a schematic describing the radius and effective radius of a hair. (c) Retrieved effective radius. (d) Correlation map between the effective radii and the cylindrical radii. Each colored dot denotes individual hairs. Boxes, median with upper and lower quartiles; whiskers, parameter range.
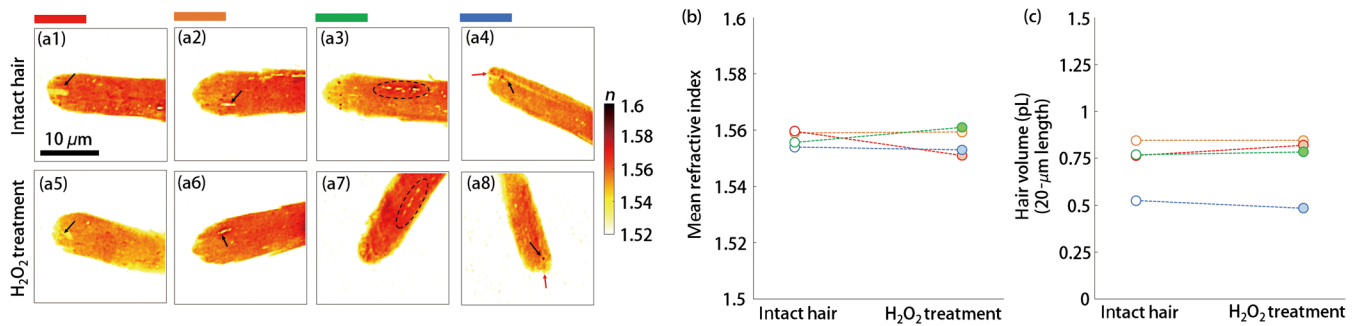
Fig. 4 Effects of hydrogen peroxide on human downy hairs. (a) *x-y* cross-sectional slices of RI tomograms for (a1)–(a4) intact hairs and (a5)–(a8) the same hairs after a 24 hr H_2O_2 treatment, respectively. (b) Mean RIs and (c) volumes of four hairs before and after the treatment. Same color denotes the same individual downy hair.

hairs. Using the present method, four hairs were systematically measured before and after a 24-h treatment with a 3% hydrogen peroxide solution (see Sec. 2). Hydrogen peroxide is one of the widely used bleaching agents which induce irreversible alterations in the physicochemical properties of the melanin granules in hair proteins.[53] It is also known that physical damage occurs to keratin proteins from oxidization.

To investigate possible alterations induced by hydrogen peroxide, we measured the morphological and biochemical properties of hairs. The *x-y* cross-sectional slices of the reconstructed 3-D RI tomograms for four intact arm hairs [Figs. 4(a1)–4(a4)] and the same hairs treated with 3% H_2O_2 [Figs. 4(a5)–4(a8)] are shown in Fig. 4(a). The arrows and the dashed region denote the same fine structures which were used to track the same hairs before and after the H_2O_2 treatment. Each graph in Figs. 4(b) and 4(c), respectively, describes the mean RIs and volumes of the 20-μm length hairs before and after H_2O_2 treatment. To retrieve these parameters, the same procedures described above were used. The mean values of RI at 532 nm for intact and H_2O_2 treated hairs were 1.557 ± 0.003 and 1.556 ± 0.005, respectively. In addition, the mean volume for the intact and H_2O_2 treated hair groups was 724 ± 141 and 731 ± 166 fL, respectively. The paired *t*-test yielded *p*-values larger than 0.5 for both the mean RI and the volume between the two hair groups, and thus does not show statistical difference before and after the treatment.

The statistical indifference between the intact hairs and the H_2O_2 treated ones, however, does not imply that the edge structures of human downy hairs are not affected by hydrogen peroxide. It seems that alterations in the edge structures of body hairs by hydrogen peroxide are small as predicted by minute morphological changes in Figs. 4(a1)–4(a8), and so are comparable with the measurement errors. Noticeably, we could not observe the black stains that may be responsible for melanin pigments at hair edges, contrary to observations at thicker parts of the hair. The absence of melanin pigments at the hair edges possibly gives rise to minute changes in the measured parameters by hydrogen peroxide.

4 Conclusion

Herein, we performed quantitative and noninvasive optical measurements on human downy arm hairs using 3-D QPI. With a Mach–Zehnder interferometer equipped with a dual axis galvanometer mirror, 3-D RI tomograms and 2-D synthetic aperture images of individual hairs were measured. To fully exploit the quantitative imaging capability of the present method, RIs and

morphological parameters including mean RI, volume, cylinder radius, and effective radius for individual downy hairs were retrieved from the measured 3-D RI maps. Finally, the RIs and morphological alterations in the downy hairs by hydrogen peroxide were also investigated with the present method.

We expect that the unique advantages of the QPI techniques with its high-resolution 3-D RI imaging capabilities can be beneficial in investigating alterations in human hairs from various chemical agents such as bleaching agents,[9,13] shampoos, and rinses. Furthermore, structural variations in hair between different human species[6,54] or gathered body sites[55,56] can also be investigated from both compositional and morphological aspects. Furthermore, recently advanced QPI techniques, including a readily implementable QPI unit,[38,57] real-time 3-D measurements,[58] spectroscopic RI imaging,[59–62] polarization-sensitive imaging,[63,64] and a super-resolution technique,[65] will also extend the applicability toward quantitative studies on the dynamic phenomena relevant to hair growths[66,67] or formations of structural defects under diverse experimental conditions.

References

1. P. E. Wheeler, "The evolution of bipedality and loss of functional body hair in hominids," *J. Hum. Evol.* **13**(1), 91–98 (1984).
2. P. E. Wheeler, "The loss of functional body hair in man: the influence of thermal environment, body form and bipedality," *J. Hum. Evol.* **14**(1), 23–28 (1985).
3. S. D. O'Connor, K. L. Komisarek, and J. D. Baldeschwieler, "Atomic force microscopy of human hair cuticles: a microscopic study of environmental effects on hair morphology," *J. Invest. Dermatol.* **105**(1), 96–99 (1995).
4. C. LaTorre and B. Bhushan, "Investigation of scale effects and directionality dependence on friction and adhesion of human hair using AFM and macroscale friction test apparatus," *Ultramicroscopy* **106**(8), 720–734 (2006).
5. S. Gurden et al., "Quantitative analysis and classification of AFM images of human hair," *J. Microsc.* **215**(1), 13–23 (2004).
6. W. Hess et al., "Human hair morphology: a scanning electron microscopy study on a male Caucasoid and a computerized classification of regional differences," *Scanning Microsc.* **4**(2), 375–386 (1990).

7. B. Lindelöf, B. Forslind, and M.-A. Hedblad, "Human hair form: morphology revealed by light and scanning electron microscopy and computer aided three-dimensional reconstruction," *Arch. Dermatol.* **124**(9), 1359–1363 (1988).

8. R. Dawber and S. Comaish, "Scanning electron microscopy of normal and abnormal hair shafts," *Arch. Dermatol.* **101**(3), 316–322 (1970).

9. T. Imai, "The influence of hair bleach on the ultrastructure of human hair with special reference to hair damage," *Okajimas Folia Anat. Jpn.* **88**(1), 1–9 (2011).

10. L. Pötsch, G. Skopp, and J. Becker, "Ultrastructural alterations and environmental exposure influence the opiate concentrations in hair of drug addicts," *Int. J. Legal Med.* **107**(6), 301–305 (1995).

11. M. Jourlin and Y. Duvault, "3D reconstruction of human hair by confocal microscopy," *J. Soc. Cosmet. Chem* **44**, 1–12 (1993).

12. C. Hadjur et al., "Cosmetic assessment of the human hair by confocal microscopy," *Scanning* **24**(2), 59–64 (2002).

13. J. Strassburger and M. M. Breuer, "Quantitative Fourier transform infrared spectroscopy of oxidized hair," *J. Soc. Cosmet. Chem* **36**, 61–74 (1985).

14. D. Ammann et al., "Degradation of the ethyl glucuronide content in hair by hydrogen peroxide and a non-destructive assay for oxidative hair treatment using infra-red spectroscopy," *Forensic Sci. Int.* **244**, 30–35 (2014).

15. Y. Miyamae, Y. Yamakawa, and Y. Ozaki, "Evaluation of physical properties of human hair by diffuse reflectance near-infrared spectroscopy," *Appl. Spectrosc.* **61**(2), 212–217 (2007)

16. X. Wang et al., "Characterization of human scalp hairs by optical low-coherence reflectometry," *Opt. Lett.* **20**(6), 524–526 (1995)

17. D. Chan et al., "Structural investigations of human hairs by spectrally resolved ellipsometry," *J. Biomed. Opt.* **11**(1), 014029 (2006)

18. A. N. Bashkatov et al., "Estimate of the melanin content in human hairs by the inverse Monte-Carlo method using a system for digital image analysis," *Quantum Electron.* **36**(12), 1111 (2006)

19. F. Pragst and M. A. Balikova, "State of the art in hair analysis for detection of drug and alcohol abuse," *Clin. Chim. Acta* **370**(1), 17–49 (2006).

20. P. Kintz, *Analytical and Practical Aspects of Drug Testing in Hair*, Taylor & Francis Group, CRC Press (2006).

21. S. Hartwig, V. Auwärter, and F. Pragst, "Effect of hair care and hair cosmetics on the concentrations of fatty acid ethyl esters in hair as markers of chronically elevated alcohol consumption," *Forensic Sci. Int.* **131**(2), 90–97 (2003).

22. V. Auwärter et al., "Fatty acid ethyl esters in hair as markers of alcohol consumption. Segmental hair analysis of alcoholics, social drinkers, and teetotalers," *Clin. Chem.* **47**(12), 2114–2123 (2001).

23. W. Baumgartner, V. Hill, and W. Blahd, "Hair analysis for drugs of abuse," *J. Forensic Sci.* **34**(6), 1433–1453 (1989).

24. G. Popescu, *Quantitative Phase Imaging of Cells and Tissues*, McGraw-Hill, New York (2011).

25. K. Lee et al., "Quantitative phase imaging techniques for the study of cell pathophysiology: from principles to applications," *Sensors* **13**(4), 4170–4191 (2013).

26. Y. Park et al., "Metabolic remodeling of the human red blood cell membrane," *Proc. Natl. Acad. Sci.* **107**(4), 1289 (2010).

27. Y. Park et al., "Measurement of red blood cell mechanics during morphological changes," *Proc. Natl. Acad. Sci.* **107**(15), 6731 (2010).

28. N. T. Shaked et al., "Quantitative microscopy and nanoscopy of sickle red blood cells performed by wide field digital interferometry," *J. Biomed. Opt.* **16**(3), 030506 (2011).

29. H. Byun et al., "Optical measurement of biomechanical properties of individual erythrocytes from a sickle cell patient," *Acta Biomaterialia* **8**(11), 4130–4138 (2012).

30. P. Memmolo et al., "3D morphometry of red blood cells by digital holography," *Cytomet. Part A* **85**(12), 1030–1036 (2014).

31. H. Park et al., "3-D refractive index tomograms and deformability of individual human red blood cells from cord blood of newborn infants and maternal blood," arXiv preprint http://arxiv.org/abs/1505.04232 (2015).

32. J. Yoon et al., "Label-free characterization of white blood cells by measuring 3D refractive index maps," arXiv preprint http://arxiv.org/abs/1505.02609 (2015).

33. H. Park et al., "Alterations in cell surface area and deformability of individual human red blood cells in stored blood," arXiv preprint http://arxiv.org/abs/1506.05259 (2015).

34. G. Popescu et al., "Optical imaging of cell mass and growth dynamics," *Am. J. Physiol.* **295**(2), C538–C544 (2008).

35. P. Jourdain et al., "Determination of transmembrane water fluxes in neurons elicited by glutamate ionotropic receptors and by the cotransporters KCC2 and NKCC1: a digital holographic microscopy study," *J. Neurosci.* **31**(33), 11846–11854 (2011).

36. Z. Wang et al., "Tissue refractive index as marker of disease," *J. Biomed. Opt.* **16**(11), 116017 (2011).

37. S. Lee et al., "High-resolution 3-D refractive index tomography and 2-D synthetic aperture imaging of live phytoplankton," *J. Opt. Soc. Korea* **18**(6), 691–697 (2014).

38. K. Kim et al., "Diffraction optical tomography using a quantitative phase imaging unit," *Opt. Lett.* **39**(24), 6935–6938 (2014).

39. V. Lauer, "New approach to optical diffraction tomography yielding a vector equation of diffraction tomography and a novel tomographic microscope," *J. Microsc.* **205**(2), 165–176 (2002).

40. M. Takeda, H. Ina, and S. Kobayashi, "Fourier-transform method of fringe-pattern analysis for computer-based topography and interferometry," *J. Opt. Soc. Am.* **72**(1), 156–160 (1982).

41. S. K. Debnath and Y. Park, "Real-time quantitative phase imaging with a spatial phase-shifting algorithm," *Opt. Lett.* **36**(23), 4677–4679 (2011).

42. S. A. Alexandrov et al., "Synthetic aperture Fourier holographic optical microscopy," *Phys. Rev. Lett.* **97**(16), 168102 (2006).

43. K. Lee et al., "Synthetic Fourier transform light scattering," *Opt. Express* **21**(19), 22453–22463 (2013).

44. V. Mico et al., "Synthetic aperture superresolution with multiple off-axis holograms," *J. Opt. Soc. Am. A* **23**(12), 3162–3170 (2006).

45. T. R. Hillman et al., "High-resolution, wide-field object reconstruction with synthetic aperture Fourier holographic optical microscopy," *Opt. Express* **17**(10), 7873–7892 (2009).

46. N. Lue et al., "Quantitative phase imaging of live cells using fast Fourier phase microscopy," *Appl. Opt.* **46**(10), 1836–1842 (2007).

47. Y. Sung et al., "Optical diffraction tomography for high resolution live cell imaging," *Opt. Express* **17**(1), 266–277 (2009).

48. K. Kim et al., "High-resolution three-dimensional imaging of red blood cells parasitized by Plasmodium falciparum and in situ hemozoin crystals using optical diffraction tomography," *J. Biomed. Opt.* **19**(1), 011005 (2014).

49. J. Lim et al., "Comparative study of iterative reconstruction algorithms for missing cone problems in optical diffraction tomography," *Opt. Express* **23**(13), 16933–16948 (2015).

50. W. Choi et al., "Tomographic phase microscopy," *Nat. Methods* **4**(9), 717–719 (2007).

51. Y. Park et al., "Refractive index maps and membrane dynamics of human red blood cells parasitized by Plasmodium falciparum," *Proc. Natl. Acad. Sci.* **105**(37), 13730 (2008).

52. M. Greenwell, A. Willner, and P. L. Kirk, "Human hair studies. III. Refractive index of crown hair," *J. Crim. Law Criminol.* **31**(6), 746–752 (1941).

53. L. J. Wolfram, K. Hall, and I. Hui, "The mechanism of hair bleaching," *J. Soc. Cosmet. Chem* **21**, 875–900 (1970).

54. A. Franbourg et al., "Current research on ethnic hair," *J. Am. Acad. Dermatol.* **48**(6), S115–S119 (2003).

55. N. Otberg et al., "Variations of hair follicle size and distribution in different body sites," *J. Invest. Dermatol.* **122**(1), 14–19 (2004).

56. O. Lunde, "A study of body hair density and distribution in normal women," *Am. J. Phys. Anthropol.* **64**(2), 179–184 (1984).

57. K. Lee and Y. Park, "Quantitative phase imaging unit," *Opt. Lett.* **39**(12), 3630–3633 (2014).

58. K. Kim et al., "Real-time visualization of 3-D dynamic microscopic objects using optical diffraction tomography," *Opt. Express* **21**(26), 32269–32278 (2013).

59. J.-H. Jung, J. Jang, and Y. Park, "Spectro-refractometry of individual microscopic objects using swept-source quantitative phase imaging," *Anal. Chem.* **85**(21), 10519–10525 (2013).

60. J. Jung et al., "Biomedical applications of holographic microspectroscopy [Invited]," *Appl. Opt.* **53**(27), G111–G122 (2014).

61. Y. Park et al., "Spectroscopic phase microscopy for quantifying hemoglobin concentrations in intact red blood cells," *Opt. Lett.* **34**(23), 3668–3670 (2009).
62. Y. Jang, J. Jang, and Y. Park, "Dynamic spectroscopic phase microscopy for quantifying hemoglobin concentration and dynamic membrane fluctuation in red blood cells," *Opt. Express* **20**(9), 9673–9681 (2012).
63. Y. Kim et al., "Polarization holographic microscopy for extracting spatio-temporally resolved Jones matrix," *Opt. Express* **20**(9), 9948–9955 (2012).
64. Z. Wang et al., "Jones phase microscopy of transparent and anisotropic samples," *Opt. Lett.* **33**(11), 1270–1272 (2008).
65. Y. Cotte et al., "Marker-free phase nanoscopy," *Nat. Photonics* **7**(2), 113–117 (2013).
66. R. Hoffmann et al., "Cytokines and growth factors influence hair growth in vitro. Possible implications for the pathogenesis and treatment of alopecia areata," *Arch. Dermatol. Res.* **288**(3), 153–156 (1996).
67. M. P. Philpott, M. R. Green, and T. Kealey, "Human hair growth in vitro," *J. Cell Sci.* **97**, 463–471 (1990).

SangYun Lee received his BS degree in physics from Korea Advanced Institute of Science and Technology (KAIST). Currently, he is a PhD student at KAIST in the Department of Physics.

Kyoohyun Kim received his BS degree in physics from KAIST. Currently, he is a PhD student at KAIST in the Department of Physics.

Yuhyun Lee is currently a student at Daejeon Dongsin Science High School. He participated in this project as part of his research and education program.

Sungjin Park is currently a student at Daejeon Dongsin Science High School. He participated in this project as part of his research and education program.

Heejae Shin is currently a student at Daejeon Dongsin Science High School. He participated in this project as part of his research and education program.

Jongwon Yang is currently a student at Daejeon Dongsin Science High School. He participated in this project as part of his research and education program.

Kwanhong Ko received his BS degree in education of physics from Korea National University of Education. Starting off as a science teacher in Jinjam Middle School, Daejeon, Korea, since 1995 he has taught in Hanbat High School, Daejeon Science High School and Daejeon High School. He is currently teaching physics at Daejeon Dongsin Science High School.

HyunJoo Park received her PhD in physics from KAIST. Since 2013, she has worked as a postdoctoral fellow at KAIST.

YongKeun Park is an associate professor in the Department of Physics, KAIST. He received his PhD in medical physics and medical engineering from Harvard-MIT Health Science and Technology in 2010, and joined KAIST. To learn more about his research projects, visit his website: http://bmol.kaist.ac.kr.